Atmos. Chem. Phys., 26, 12183–12196, 2026
https://doi.org/10.5194/acp-26-12183-2026

Atmospheric Chemistry and Physics
Open Access
EGU

In situ real-time determination of SO_2 photochemical oxidation in nanoscale sea salt aerosols based on dark-field microscopy

Xijie Xiong[1], Zhibo Xie[1], Xiuli Wei[1], Douguo Zhang[2], Jianguo Liu[1], and Huaqiao Gui[1,3]

[1]Key Laboratory of Environmental Optics and Technology, Anhui Institute of Optics and Fine Mechanics, Chinese Academy of Sciences, Hefei 230031, China
[2]Institute of Photonics, Department of Optics and Optical Engineering, University of Science and Technology of China, Hefei, Anhui 230026, China
[3]Institute of Environment, Hefei Comprehensive National Science Center, Hefei 231299, China

Correspondence: Zhibo Xie (zbxie@aiofm.ac.cn) and Huaqiao Gui (hqgui@aiofm.ac.cn)

Received: 8 January 2026 – Discussion started: 27 January 2026
Revised: 10 June 2026 – Accepted: 20 July 2026 – Published: 28 August 2026

Abstract. Heterogeneous reaction processes of aerosols play an important role in air quality and climate change. However, the lack of in-situ measurements of single-nanoparticle reactions results in large uncertainties in modeling the nanoparticle reaction kinetics. The study introduces a method to quantify reaction rates of single-nanoparticles using hygroscopic growth factors (GFs) and the Zdanovskii-Stokes-Robinson (ZSR) rule. Planar waveguide dark-field microscopy was employed to monitor sodium chloride (NaCl) aerosol GFs under ultraviolet (UV) irradiation and SO_2 exposure in real time. The results revealed a first-order reaction rate constant of $0.6523\,h^{-1}$ for 100 nm NaCl aerosols. Moreover, the reaction rate constant exhibits a non-monotonic size dependence on particle diameter-increasing in the 50–200 nm range and decreasing for particle sizes larger than 200 nm. This reflects a competitive interplay between the surface curvature effect at small particle sizes and specific surface area effect at larger sizes, which is further validated by a combined analysis based on transition state theory and the double-film mass transfer approach. Subsequently, sodium octyl sulfate (SOS) was introduced to form binary NaCl-based nanoaerosols, where the organic coating content was systematically varied under constant surface curvature to modulate the specific surface area. An increase in organic volume fraction (OVF) reduces the effective specific surface area and suppresses heterogeneous reaction rates, accompanied by a pronounced nonlinear transition from partial to complete coating. This further confirms the experimentally observed size-dependent nonlinearity in reaction rates and offers new insights into nanoscale sulfate formation, improving atmospheric chemical models and pollution-climate assessments.

1 Introduction

Aerosol–atmosphere interactions are central to Earth's climate system and air quality (Carslaw et al., 2010; Li et al., 2024). Tropospheric aerosols not only scatter and absorb solar radiation but also serve as active media for multiphase oxidation reactions, which alter their chemical composition and physicochemical properties such as hygroscopicity and refractive index (Bi et al., 2013). These changes can significantly influence atmospheric visibility, cloud and fog formation, and wet deposition processes (Cui et al., 2016; Persad, 2023). Under ambient sunlight, aerosols are exposed to oxidants such as ozone (O_3), hydroxyl radicals (•OH), and reactive chlorine species (ClO_x) (Ma et al., 2010; Shang et al., 2021). These heterogeneous reactions drive compositional and morphological changes that modify optical and hygroscopic properties, enhance secondary pollutant formation, and regulate atmospheric oxidative capacity (Laskin et al., 2012; Keene et al., 1998; Rossi, 2003; Cao et al., 2023, 2024a; Jing et al., 2023). However, most previous studies fo-

cused on micrometer-scale droplets or bulk systems, while the kinetics of photochemical SO_2 oxidation in nanoscale sea-salt aerosols remain poorly constrained. In nanoscale droplets, geometric factors such as surface-to-volume ratio and surface curvature may substantially alter interfacial transport and heterogeneous reaction kinetics (Barclay and Lukes, 2019). Notably, surface-catalyzed oxidation of S(IV) by Mn(III) at droplet interfaces can proceed two to three orders of magnitude faster than bulk-phase reactions, and neglecting such interfacial processes in models may substantially underestimate aerosol aging and cloud condensation nuclei (CCN) activity. These observations highlight the need for kinetic descriptions that incorporate particle-size and interface effects (Rosati et al., 2021; Wang et al., 2021; Gen et al., 2020; Liu and Abbatt, 2021; Yang et al., 2023).

Traditional characterization of heterogeneous reaction kinetics is typically performed using laboratory-based flow reactors or smog chambers (Liu et al., 2020). For instance, the sulfate formation rate from the aqueous oxidation of SO_2 (or H_2O_2) can be determined offline after a given reaction time in an aerosol flow reactor, yielding kinetic parameters that represent the ensemble-averaged behavior of the aerosol population during the reaction process. To investigate the kinetics of individual suspended micrometer-sized aerosol particles, Aerosol Optical Tweezers (AOT) have been developed (Angle et al., 2021). When combined with cavity-enhanced Raman spectroscopy, this technique enables the direct measurement of the kinetics of Fe(III)-catalyzed SO_2 heterogeneous oxidation within micrometer-sized droplets. The Raman signal, which reflects the temporal evolution of reactant or product concentrations, can be quantitatively correlated with reaction rates. This approach has been applied to elucidate mechanisms of sulfate formation via transition-metal-catalyzed oxidation on sea-salt aerosol surfaces and to explore the influence of environmental factors on such interfacial processes. However, the determination of reaction kinetics for single nanometer-sized aerosol particles still remains challenging at present (Xie et al., 2023). A photonic-chip-based dark-field imaging technique has recently been reported for the in situ observation of nanoscale aerosols, enabling stable detection of particles as small as 50 nm across centimeter-scale fields of view. Individual particles deposited on the substrate can be monitored continuously for hours to days, while an integrated reaction chamber permits precise control of gas composition, humidity, and temperature. This approach facilitates direct measurements of nanoscale heterogeneous reaction kinetics and their dependence on particle properties such as specific surface area and curvature, overcoming both the diffraction limitations of conventional optical methods and the incompatibility of electron microscopy with dynamic atmospheric environments (Kuai et al., 2019, 2020; Xie et al., 2020).

Sea-salt aerosols constitute the largest mass fraction of natural atmospheric aerosols, and the contribution of nanometer-sized particles during atmospheric transport is non-negligible (Chi et al., 2015; Gong et al., 2023; Murphy et al., 2019). Their major component, sodium chloride, undergoes chemical transformation during transport from marine to continental regions under clear-sky conditions. Chloride ions released from sea-salt particles can form a series of reactive chlorine compounds (Su et al., 2022; Rossi, 2003; Finlayson-Pitts and Hemminger, 2000), which significantly enhance the oxidative capacity of the atmosphere and promote the formation of secondary pollutants such as sulfate and nitrate (Wang et al., 2019; Zhang et al., 2021; Soni et al., 2023; Cao et al., 2024b). Sea-salt particles frequently coexist with organic species to form mixed organic–inorganic aerosols, which often exhibit nonideal phase behavior such as liquid-liquid phase separation (LLPS) (Freedman, 2017, 2020; Zhang et al., 2022). The formation of an organic shell can hinder the diffusion of reactive gases (e.g., HNO_3, SO_2) into the inorganic core, thereby strongly affecting the kinetics of heterogeneous reactions.

In this study, we quantify the reaction rate of SO_2 photooxidation on nanoscale sea-salt aerosol droplets under UV irradiation by combining hygroscopic GF with the ZSR mixing rule. The GFs were obtained in real time using planar-waveguide dark-field microscopy under controlled UV and SO_2 exposure. By resolving the size-dependent kinetics in the 50–400 nm regime, we elucidate how nanoscale curvature and specific surface area jointly regulate heterogeneous reactivity, thereby providing quantitative constraints on the contribution of ultrafine sea-salt aerosols to the atmospheric sulfur cycle. In addition, by simulating surface modification through organic sulfonate coatings, we assess how reduced equivalent specific surface area suppresses reaction rates, offering direct experimental evidence for sulfate formation pathways in complex atmospheric systems, including marine-organic mixtures and anthropogenically influenced aerosols. Collectively, these findings provide new insight into the mechanisms driving rapid sulfate production during haze episodes and improve our ability to predict how anthropogenic surfactant emissions may indirectly alter atmospheric chemistry by modifying aerosol surface reactivity.

2 Methods

2.1 Sample Preparation

The chemical reagent NaCl used for preparing nanoscale particulate aerosol particles was purchased from Sinopharm Chemical Reagent Co., Ltd. (Shanghai, China). A standard solution with a concentration of $1.0\,g\,L^{-1}$ was prepared using ultrapure water from a Millipore Direct-Q3 system (Merck, Darmstadt, Germany). The standard solution was aerosolized into ultrafine aerosol particles with a particle size of approximately 50–400 nm using an aerosol generation system, which consists of a MetOne 255 nebulizer, a silica gel diffusion dryer (to achieve a final relative humidity (RH) of $< 5\,\%$), a TSI 3081 differential mobility analyzer, and a TSI

3080 platform (as shown in Fig. 1). Monodisperse particles collided and deposited on the substrate surface in the sample chamber for 20 min. To minimize potential substrate-induced photocatalytic effects, the SiO_2 substrate was coated with a thin inert Au layer prior to the experiments. Mixed NaCl-SOS particles were generated from NaCl-SOS solutions with a prescribed mass ratio of 38 : 1, 18 : 1, 8 : 1, 4 : 1, 2 : 1 and 1 : 1 (OVF5 %, 10 %, 18 %, 33 %, 50 %, and 70 %).

2.2 Sample Humidification and Aging

The RH was controlled using a humidifier, a dryer, and a proportional-integral-derivative (PID) controller, as shown in Fig. 1. The PID controller fed back a pulse signal to a three-way solenoid valve based on the desired and measured RH. The required RH was achieved by mixing dry and wet gases. During the photo-aging process, the sample underwent heterogeneous reactions with SO_2. The reaction gases, nitrogen (N_2, Qingjie Chemical Trading Co., Hefei, China) and sulfur dioxide (SO_2, containing ppm levels of SO_2 in nitrogen; Qingjie Chemical Trading Co., Hefei, China), were supplied by gas cylinders, with flow rates controlled by mass flow meters to provide the desired SO_2 concentration. The gas containing the desired SO_2 concentration was mixed with the gas at the required RH using a mixer, as shown in Fig. 1, and then passed into the sample chamber containing the deposited particles. The carrier gas consisted of SO_2, N_2, and water vapor. O_2 was not intentionally introduced into the system. This design was adopted to control experimental variables and to better highlight geometric effects associated with particle size and curvature. An RH of 85 % was selected to ensure that NaCl particles remained in an aqueous state and to facilitate efficient mass transfer and photochemical oxidation under humid conditions relevant to polluted environments (Rosati et al., 2021). An SO_2 concentration of 200 ppm, although higher than typical atmospheric background levels, was adopted to simulate extreme pollution scenarios (e.g., industrial plumes or severe pollution events) and to provide sufficient signal for robust single-particle kinetic analysis within the experimental time scale (Yang et al., 2023). A UV light source was placed above the sample chamber (365–370 nm, 5 W) for effective simulation of daytime atmospheric photochemical processes. After the set reaction time, dry gas was injected into the sample chamber for 10 min to dry the particles, after which their hygroscopicity was measured. The reaction-rate calculation method used in this work was validated by ion chromatography (IC). Particles produced from the pure NaCl solution described in Sect. 2.1 were collected on quartz fiber filters (81 mm; TE-20-3010Z, Tisch Environmental) using a particle sampler, and subsequently aged under the same conditions. After aging, the filters were cut into small pieces and extracted in ultrapure water. The concentrations of anions formed during aging were quantified by IC using a Dionex ICS-3000 system (Thermo Fisher Scientific). NaCl-SOS mixed particles were subjected to a humidification–drying cycle to induce LLPS, following the procedure reported by Zhang et al. (2022). After LLPS formation, the mixed particles were aged under SO_2 concentrations and UV irradiation intensities identical to those used for pure NaCl. For each OVF, particles were exposed to reaction times of 2 and 3 h, respectively.

2.3 Measurement System

The measurement system illustrated in Fig. 1 is based on a photonic-chip-enabled evanescent-wave illumination scheme combined with dark-field optical imaging, which allows in situ characterization of individual aerosol nanoparticles down to the nanometer scale. The photonic chip consists of a three-layer architecture designed to selectively manipulate the propagation and scattering of incident light. The middle layer is a $\sim 2\,\mu m$ thick dielectric film embedded with ~ 60 nm titanium dioxide (TiO_2) nanoparticles, which act as efficient scattering centers. The top and bottom layers are dielectric multilayer stacks composed of alternating silica (SiO_2) and silicon nitride (SiN_x) films, engineered to exhibit distinct photonic band gaps (PBGs). The optical reflectance of both multilayer stacks was calculated using the transfer matrix method, as detailed in Kuai et al. (2020). For the bottom multilayer, a reflection minimum occurs near normal incidence for both transverse electric (TE) and transverse magnetic (TM) polarized light, such that only light propagating close to 0° can be transmitted at the design wavelength of 750 nm. Upon entering the TiO_2-doped scattering layer, the transmitted light undergoes multiple scattering events, resulting in a redistribution of propagation directions. Scattered light incident on the bottom multilayer outside the narrow transmission window is reflected back into the scattering layer by the PBG, while only near-normal components are allowed to exit. The top multilayer is designed with a PBG centered at 750 nm, permitting transmission only for scattered light within a limited angular range. Scattered light with propagation directions exceeding a numerical aperture (NA) of 0.7 is reflected back into the scattering layer. Consequently, when an objective lens with NA < 0.7 is used, background illumination is effectively suppressed, enabling dark-field imaging. For illumination at 640 nm, the scattered light lies within the photonic band gap of the multilayer structure; when the scattering angle exceeds the critical angle, evanescent waves are generated at the multilayer–air interface. Aerosol particles deposited on the surface of the top multilayer are selectively illuminated by these evanescent waves, producing high-contrast images with minimal background interference. This optical configuration enables sensitive detection of individual aerosol nanoparticles and allows continuous monitoring of their hygroscopic growth under controlled environmental conditions. During hygroscopicity measurements, surface-wave images are recorded at each prescribed relative humidity (RH). The grayscale intensity of individual particles is extracted through image anal-

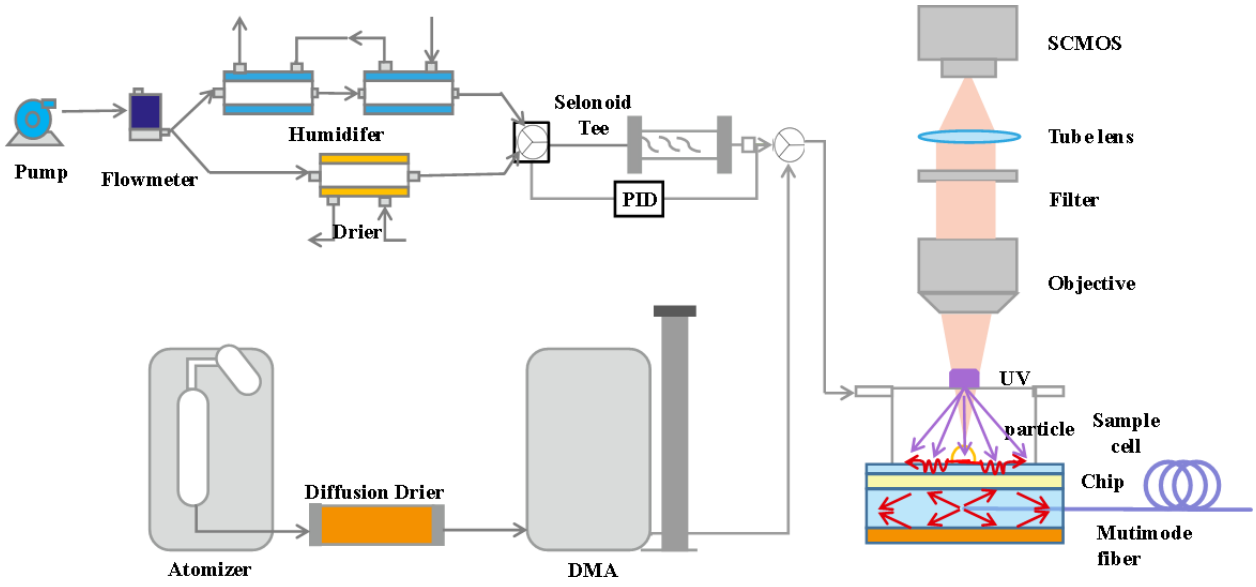

Figure 1. Schematic diagram of the system for generation, aging, and hygroscopic growth measurements based dark-field imaging for single nanoparticles.

ysis, and the cube root of the normalized intensity is used to derive the hygroscopic growth factor (GF), as validated in Kuai et al. (2020). Importantly, the compact photonic-chip platform can be readily integrated with a series of upstream reaction chambers, enabling sequential exposure of the same individual particles to dynamically controlled environments, including changes in RH, gas-phase composition, and irradiation conditions. This configuration allows real-time, single-particle tracking of physicochemical transformations in aerosol nanoparticles during hygroscopic growth, phase transitions, and heterogeneous or photochemical reactions, providing a unique capability for simulating complex atmospheric processes under well-defined and time-resolved conditions

$$\frac{\sqrt[3]{\text{Gray}_{\text{wet}}}}{\sqrt[3]{\text{Gray}_{\text{dry}}}} = \frac{D_{\text{wet}}}{D_{\text{dry}}} = \text{GF} \tag{1}$$

where Gray_{wet} and Gray_{dry} represent the gray signal intensity of the surface wave image of the nanoparticles before and after humidification, and D_{dry} and D_{wet} represent the particle sizes before and after humidification. The reliability of the measurement method was evaluated using hygroscopic growth measurements of single 100 nm NaCl particles, with the results (Fig. 2) showing good agreement with predictions from the thermodynamic model E-AIM.

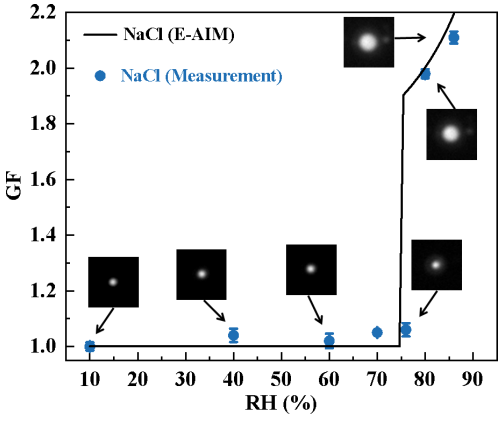

Figure 2. Hygroscopic growth behavior of a single 100 nm NaCl particle.

2.4 Retrieval of reaction progress and kinetic parameters

Based on the ZSR volume-weighted mixing rule, it is assumed that the components in the mixed particles retain their independent hygroscopic properties (Zangmeister and Pemberton, 2000). The hygroscopic GF of the mixed-component nanoparticles can be expressed as:

$$\text{GF}_{\text{mixed}} = \left(\sum_{i}^{n} \epsilon_i \text{GF}_i^3\right)^{1/3} \tag{2}$$

$$\epsilon_i = \frac{w_i/\rho_i}{\sum_{k}^{n} \frac{w_k}{\rho_k}} \tag{3}$$

where GF_i is the hygroscopic growth factor of the pure component i, ϵ_i is the volume fraction of the pure component i in the dry state, and n is the number of pure components.

For a given reaction system, two reference compositional states were defined: the initial state and the final state. The initial state corresponds to the particle composition before reaction, whereas the final state corresponds to the composition reached after prolonged reaction, when no further measurable change in hygroscopic behavior is observed. The composition of a particle at reaction time t was assumed to be represented by a linear combination of these two end-member states, therefore the hygroscopic behavior of a particle at reaction time t was assumed to be represented by a volume-weighted combination of the initial and final end-member states:

$$\mathrm{GF}_t = \left[(1-\epsilon)\mathrm{GF}_0^3 + \epsilon \mathrm{GF}_\infty^3\right]^{1/3} \tag{4}$$

Where GF_t is the hygroscopic growth factor measured at reaction time t, GF_0 is the hygroscopic growth factor of the initial-state particle, GF_∞ is the hygroscopic growth factor of the final-state particle after the reaction reaches a steady state, and ϵ represents the dry-volume fractions of the final-state composition and can be interpreted as the reaction progress variable, which can obtain from Eq. (4):

$$\epsilon = \frac{\mathrm{GF}_t^3 - \mathrm{GF}_0^3}{\mathrm{GF}_\infty^3 - \mathrm{GF}_0^3} \tag{5}$$

By definition, ϵ varies between 0 and 1, corresponding to the initial-state and final-state end members, respectively. Using the retrieved dry-volume fractions together with the measured hygroscopic growth factor, the concentrations of reactant and product species in the droplet phase were calculated. The concentration of each species was calculated by converting its dry-volume fraction into molar amount and normalizing by the droplet volume at the corresponding RH:

$$C_\mathrm{R}(t) = \frac{(1-\epsilon)V_t\rho_\mathrm{R}}{M_\mathrm{R}V_{t,\mathrm{RH}}} = \frac{\rho_\mathrm{R}(1-\epsilon)}{M_\mathrm{R}\mathrm{GF}_{t,\mathrm{RH}}^3} \tag{6}$$

Where $C_\mathrm{R}(t)$ is the concentration of the reactant species in the aqueous droplet at reaction time t, V_t is the dry particle volume at reaction time t, ρ_R is the density of the reactant phase, M_R is the molar mass of the reactant, and $V_{t,\mathrm{RH}}$ is the droplet volume at the corresponding RH. Since the droplet volume can be expressed as:

$$V_{t,\mathrm{RH}} = \mathrm{GF}_{t,\mathrm{RH}}^3 V_t$$

Equation (6) can be simplified to the expression on the right-hand side, where $\mathrm{GF}_{t,\mathrm{RH}}$ is the hygroscopic GF of the particle at reaction time t and RH.

$$C_\mathrm{P}(t) = \frac{\epsilon V_t\rho_\mathrm{P}}{M_\mathrm{P}V_{t,\mathrm{RH}}} = \frac{\rho_\mathrm{P}\epsilon}{M_\mathrm{P}\mathrm{GF}_{t,\mathrm{RH}}^3} \tag{7}$$

Where $C_\mathrm{P}(t)$ is the concentration of the sulfate-containing products in the aqueous droplet at reaction time t, ρ_P is the density of the reaction products, and M_P is the corresponding molar mass. For the present system, M_P and ρ_P were assigned according to the dominant sulfate-containing product identified in the final-state particles.

For the NaCl–SO_2system investigated here, the initial-state end member corresponds to pure NaCl particles. Therefore, ϵ represents the residual dry-volume fraction of NaCl, while $1-\epsilon$ represents the dry-volume fraction of sulfate-containing products.

The temporal evolution of the retrieved NaCl concentration was then used to evaluate the reaction kinetics. Assuming pseudo-first-order kinetics with respect to reactant consumption, the apparent rate constant k was obtained from the slope of the linear regression between and reaction time:

$$\ln\left(\frac{C_0}{C_t}\right) = kt$$

where C_0 and C_t are the NaCl concentrations at the initial state and at reaction time t, respectively, and k is the apparent pseudo-first-order rate constant.

It should be noted that this end-member approach does not require prior specification of individual reaction products and may be therefore applicable to systems in which the product composition evolves continuously during reaction.

2.5 Control of Biphase Droplet Phase State

To study the effect of droplet surface area on the reaction rate, we introduced SOS to cover the surface of the droplets. Therefore, we selected six OVF values (5 %, 10 %, 18 %, 33 %, 50 %, and 70 %) for the experiments to investigate the impact of a decrease in the specific surface area of nano-droplets on the gas-liquid reaction rate when the interface curvature is constant. This also provides a method for determining the phase state of nano biphase droplets. Six OVF values for the binary particles were tested after 2 and 3 h reaction times. The results were used to calculate the hygroscopic GF of the components of the binary particle, excluding SOS. Furthermore, the hygroscopic growth curves for NaCl and $NaHSO_4$ were obtained using the E-AIM model, based on Köhler theory.

3 Results and Discussion

3.1 Reaction Rate Measurement

3.1.1 Hygroscopic Growth Factor Measurement

NaCl particles were exposed to 85 % RH and UV irradiation, allowing it to undergo photochemical aging reactions with SO_2 gas. The aerosol was then dried, followed by humidification from 25 % RH to 85 % RH under reaction times of 1, 2, 3, 4, and 5 h. The corresponding microscopic images of the NaCl particles after different reaction times are presented in Figs. S1–S5 in the Supplement. The results are shown in

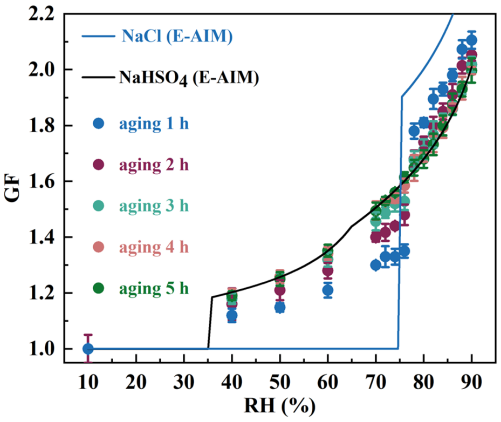

Figure 3. GFs of 100 nm NaCl particles after reaction times of 1, 2, 3, 4, and 5 h, together with the predicted GFs of NaCl and $NaHSO_4$.

Fig. 3, each data point represents the average value of GF measured for single particles at three randomly selected positions, with the standard deviation shown as error bars As shown in Fig. 3, the hygroscopicity of NaCl particles in response to SO_2 absorption exhibited different behaviors under low RH (< 78 % RH) and high RH (> 78 % RH).

When RH was less than 78 % RH (the deliquescence relative humidity (DRH) of NaCl), the reaction caused an increase in the hygroscopicity of NaCl particles. As shown in Fig. 3, compared to fresh NaCl particles (represented by blue curve), the reaction products generally exhibited hygroscopicity at RH values below 78 %, with the increase in hygroscopicity becoming more pronounced with longer reaction times. After 4 h of reaction, the hygroscopicity of the aerosols began to stabilize. When RH exceeded 78 % RH, the reaction caused a decrease in the hygroscopicity of NaCl aerosols. The hygroscopicity of the aged particle decreased at RH values above 78 %, and the reduction in hygroscopicity became more pronounced with longer reaction times. Similar to the low RH scenario, the hygroscopicity began to stabilize after 4 h of reaction.

The product of the oxidation reaction between NaCl and SO_2 could be Na_2SO_4 or $NaHSO_4$ (Wang et al., 2018), but the former is a substance with a higher DRH and stronger hygroscopicity upon deliquescence compared to NaCl, which is inconsistent with the measurements in this work. To determine the nature of the reaction products, we used the E-AIM model to predict the hygroscopic curve of $NaHSO_4$, which is shown by the black curve in Fig. 3, GF measurements of pure $NaHSO_4$ particles were conducted under the same experimental conditions to further validate the E-AIM-based analysis, The measured GFs agreed well with the corresponding E-AIM predictions (Fig. S21). This was compared with the GF measurements of the aged particle, and the predicted hygroscopic curve of NaCl. It can be seen that, at the same RH, the GF measurements of the aged aerosol moved towards the $NaHSO_4$ curve with increasing reaction time, moving away from the NaCl curve, and ultimately stabilizing near the $NaHSO_4$ curve. Based on this, we conclude that the reaction product is $NaHSO_4$.

In conclusion, under 85 % RH and UV light conditions, NaCl aerosols absorb SO_2 and produce $NaHSO_4$. The DRH of $NaHSO_4$ is 35 %, which allows the aged aerosol to exhibit hygroscopicity at low RH. At high RH, $NaHSO_4$ exhibits lower hygroscopicity than deliquescent NaCl, leading to a decrease in the hygroscopicity of aged aerosols at high RH. The longer the reaction time, the more $NaHSO_4$ is formed, resulting in stronger hygroscopicity at low RH and weaker hygroscopicity at high RH in the aged aerosols.

We observed that the evolution of aerosol hygroscopicity slowed with increasing reaction time. Compared to fresh NaCl aerosols, the GF of aged aerosols at 60 % RH increased by 14 %, 23 %, 30 %, 34 %, and 35 % after reaction times of 1, 2, 3, 4, and 5 h, respectively. After 4 h of reaction, the GF showed little further increase. At 80 % RH, the GF decreased by 7.5 %, 11.4 %, 14.9 %, 15.9 %, and 16.4 % after reaction times of 1, 2, 3, 4, and 5 h, respectively, and after 4 h of reaction, the GF showed little further decrease. This indicates that ultraviolet-catalyzed SO_2 uptake and sulfate formation in NaCl particles are time-dependent, with the reaction rate decreasing as the reaction proceeds.

3.1.2 Reaction Rate Constant Calculation

We calculated the sulfate formation ($mol\,L^{-1}$) for droplets formed by 100 nm NaCl dry particles at fixed relative humidity (85 % RH) and SO_2 concentration (200 ppm) after different reaction times. The calculation results are shown in Fig. 4a. Each data point represents the mean sulfate formation derived from single-particle GF measurements conducted at six different RHs, with the corresponding standard deviations shown as error bars. Sulfate formation increased monotonically with reaction time, exhibiting a rapid increase during the initial stage followed by a gradual deceleration as the reaction progressed. After approximately 4 h, sulfate formation approached a plateau, suggesting that the reaction was nearing completion. The temporal evolution of sulfate formation is well described by an exponential function, indicating kinetically limited behavior. Consistent with this observation, the residual NaCl content within the droplet was quantified and plotted as $\ln(C_0/C)$ versus reaction time (Fig. 4b). To evaluate the reaction kinetics, the residual NaCl concentration was analyzed using $\ln(C_0/C)$. As NaCl serves as the reactant, its concentration decreased exponentially with increasing reaction time. In the logarithmic space, $\ln(C_0/C)$ exhibited a linear dependence on time, yielding a slope of 0.6523, with the shaded region representing the 95 % confidence interval of the fitted curve. This behavior is consistent with a pseudo-first-order reaction with respect to NaCl, corresponding to an apparent rate constant of approximately $0.6523\,h^{-1}$. Independent validation was obtained from IC, to facilitate a direct comparison with the

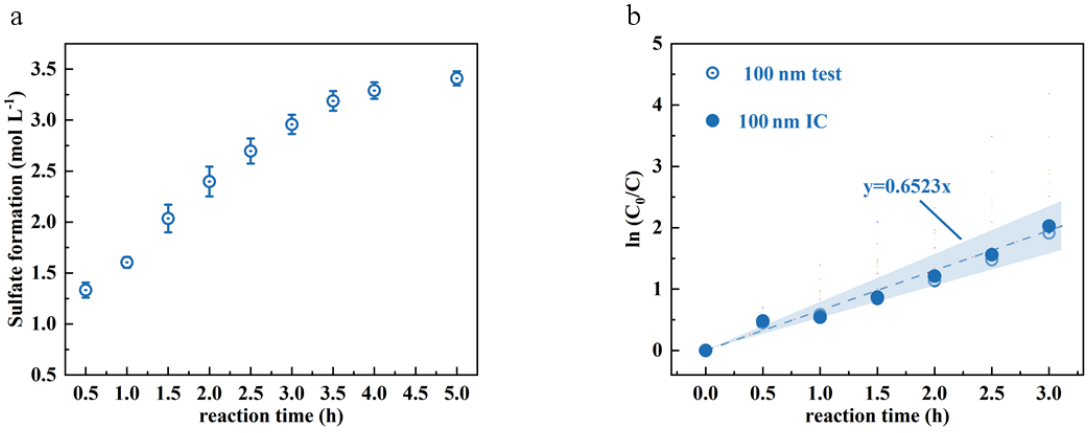

Figure 4. **(a)** Sulfate concentration and **(b)** $\ln(C_0/C)$ of 100 nm NaCl droplets formed at 80 % RH as a function of reaction time.

measurements, the IC data were converted accordingly. In IC analysis, the ratio of the characteristic peak areas of sulfate and chloride ions is proportional to the ratio of their concentrations:

$$\frac{A_{SO_4^{2-}}}{A_{Cl^-}} = \frac{C_{SO_4^{2-}}}{C_{Cl^-}} \tag{8}$$

where $A_{SO_4^{2-}}$ and A_{Cl^-} represent the IC peak areas of sulfate and chloride ions, respectively, and $C_{SO_4^{2-}}$ and C_{Cl^-} denote their corresponding concentrations. In our calculation framework, the concentrations of sulfate and chloride ions in the droplet after a reaction time t can be expressed as:

$$C_{SO_4^{2-}} = \frac{\rho_{NaHSO_4}(1-\epsilon)}{M_{NaHSO_4} GF_{t,RH}^3} \tag{9}$$

$$C_{Cl^-} = \frac{\rho_{NaCl}\epsilon}{M_{NaCl} GF_{t,RH}^3} \tag{10}$$

where ρ_{NaHSO_4} and ρ_{Cl^-} represent the density of the $NaHSO_4$ and NaCl, and M_{NaHSO_4} and M_{Cl^-} represent the molar mass of the $NaHSO_4$ and NaCl. In this study, the natural logarithm of the ratio of the reactant concentration (NaCl) to its initial concentration was used as a metric to characterize the progression of the reaction:

$$\ln\frac{C_0}{C} = \ln\frac{GF_{t,RH}^3}{GF_{0,RH}^3\epsilon} \tag{11}$$

By combining Eqs. (8)–(11) can obtain:

$$\ln\frac{C_0}{C} = \ln\left[\frac{GF_{t,RH}^3}{GF_{0,RH}^3}\left(\frac{\rho_{NaCl}M_{NaHSO_4}}{\rho_{NaHSO_4}M_{NaCl}}\frac{A_{SO_4^{2-}}}{A_{Cl^-}} + 1\right)\right] \tag{12}$$

The IC measurement results used for validation are shown in Fig. S19. The IC-derived data show a consistent linear trend, corroborating the GF-based analysis and confirming the concurrent formation of sulfate and the consumption of NaCl. This demonstrates that the combination of GF measurements and the ZSR mixing rule provides a reliable approach for inferring reaction kinetics in aerosol nanoparticles.

To assess whether the observed kinetic behavior is sensitive to the elevated SO_2 concentration employed in this study, an additional control experiment was conducted using 100 nm NaCl particles at a lower SO_2 concentration of 20 ppm under otherwise identical experimental conditions (85 % RH and UV irradiation). The corresponding hygroscopic growth measurements and kinetic analysis are provided in the Supplement (Fig. S20). The derived apparent first-order rate constant was 0.2254 h^{-1}, lower than the value obtained at 200 ppm SO_2 (0.6523 h^{-1}), indicating that the reaction rate decreases with decreasing SO_2 concentration. Nevertheless, the reaction remained well described by first-order kinetics, and the overall temporal evolution of sulfate formation was consistent with that observed at higher SO_2 levels. These results suggest that although the absolute reaction rate affected by SO_2 concentration, the kinetic framework developed in this study remains applicable across a range of SO_2 concentrations.

3.2 Size Dependence of Reaction Rates

From a kinetic perspective, bulk-phase reactions at constant RH are expected to exhibit size-independent reaction rates, whereas surface reactions should scale inversely with particle radius ($1/r$). To examine the role of particle size, sulfate formation was monitored as a function of time for NaCl particles with diameters ranging from 50 to 400 nm under UV-induced oxidation of SO_2 at 85 % RH. The representative particle images for different particle sizes and reaction conditions are provided in Figs. S6–S12, and the GF values derived from these single-particle images are summarized in Table S1. The temporal evolution of sulfate formation and the corresponding $\ln(C_0/C)$ values of residual NaCl for different particle sizes are shown in the Fig. 5. Each data point in Fig. 5a and b represents the average value of sulfate forma-

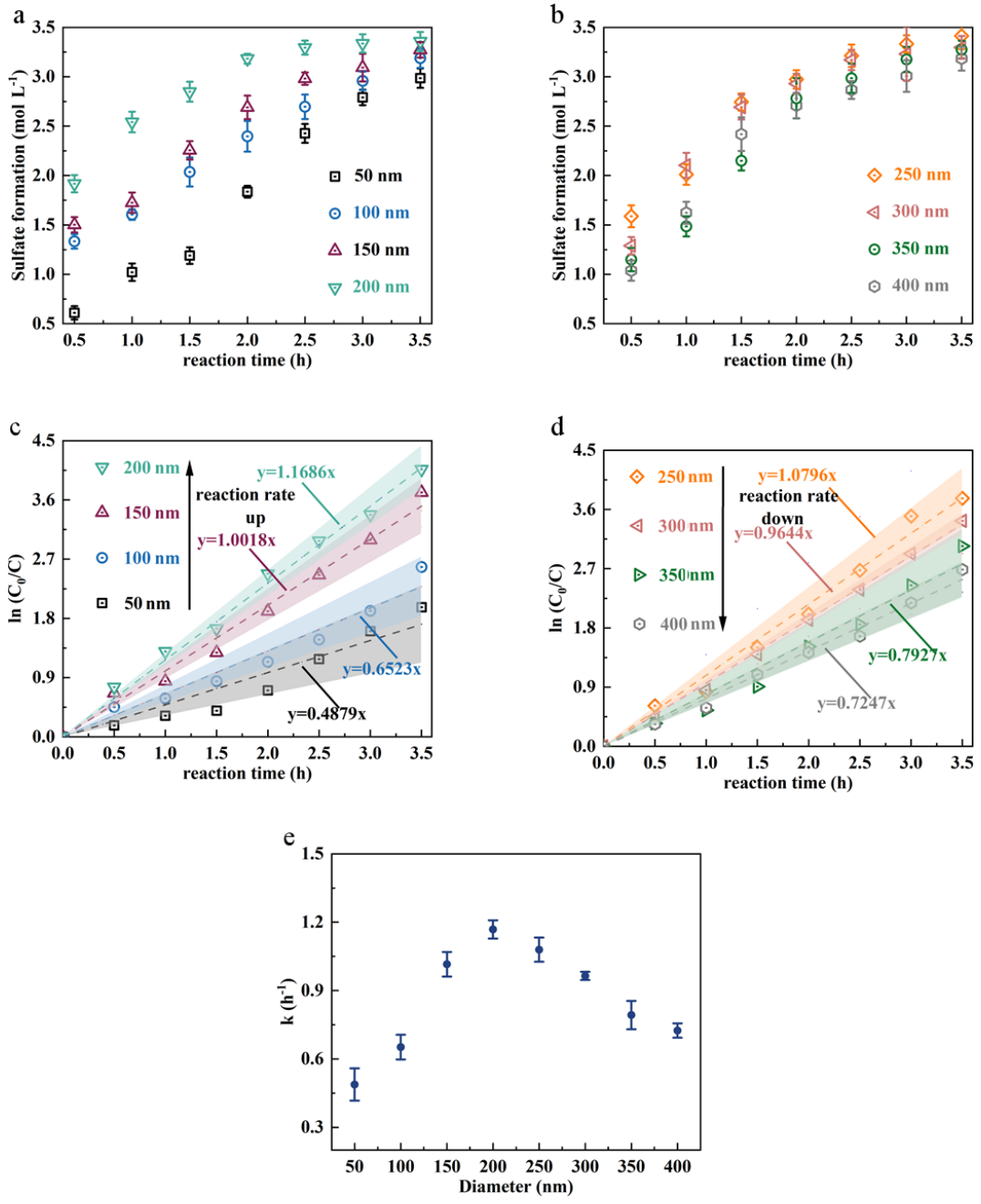

Figure 5. **(a–b)** Sulfate concentration and **(c–d)** $\ln(C_0/C)$ of 50–400 nm NaCl droplets formed at 80 % RH under different reaction times. **(e)** Relationship between k and dry diameters of particles.

tion calculated from single-particle GF measurements conducted at six different RHs, with standard deviations represented as error bars. The shadow in Fig. 5c and d represents the 95 % confidence interval of the fitted curve. Overall, sulfate formation and NaCl consumption exhibit similar kinetic behaviors to those observed for the 100 nm particles. For a given reaction time, the sulfate formation depends on particle size, reaching a maximum for particles with a diameter of approximately 200 nm. Sulfate production increased with particle size in the range of 50–200 nm, whereas a decreasing trend was observed for particles between 200 and 400 nm. Consistent with these observations, the $\ln(C_0/C)$ plots of NaCl residuals display size-dependent slopes, indicating that the apparent rate constants k varies with particle size. The highest k value was obtained for the 200 nm particles, revealing a non-monotonic dependence of reaction kinetics on particle size: k increased with particle size for particles smaller than 200 nm, but decreased for larger particles.

The observed non-monotonic dependence of sulfate formation kinetics on particle size reflects the coexistence of distinct kinetic regimes across the nano- to microscale. For nanoscale NaCl aerosols, the heterogeneous photochemical oxidation of SO_2 is governed primarily by interfacial and near-surface transport processes, whereas for larger droplets, surface-area limitations and bulk-phase diffusion progressively dominate the reaction kinetics. For particles with diameters between 50 and 200 nm, the apparent reaction rate increases with particle size. This behavior can be attributed to curvature-related effects that suppress gas uptake and interfacial transport in very small droplets. According to Köhler theory, the increasing of the equilibrium vapour pressure above a curved droplet surface caused by decreasing radius due to the Kelvin effect renders net condensation and uptake thermodynamically less favorable for very small droplets (Kaku et al., 2006; Davies et al., 2019). In parallel, experimental and modeling studies have shown that the mass-accommodation (or uptake) coefficient decreases with increasing surface curvature, leading to reduced gas-to-particle fluxes for nanometer-sized droplets (Barclay and Lukes, 2019). Kinetic multilayer models demonstrate that reduced accommodation or weakened surface driving forces directly translate into lower heterogeneous reaction rates when interfacial or near-surface transport becomes limiting (Shiraiwa et al., 2010; Chan and Chan, 2005). As a result, smaller particles (e.g., 50 and 100 nm) require longer equilibration times, consistent with the reduced sulfate formation rates in this size range. As particle size increases toward 200 nm, the influence of curvature diminishes, facilitating more efficient gas uptake and enhancing the apparent reaction rate.

To rationalize the experimentally observed non-monotonic size dependence of the apparent reaction rate constant, we develop a mechanistic framework that integrates transition state theory with a two-film-type resistance model. This approach enables a quantitative assessment of how curvature-modified interfacial reactivity and finite transport limitations jointly give rise to an optimal particle size. Following transition state theory, the probability (or rate coefficient) for gas–surface uptake can be written as an activated process,

$$\alpha \propto \exp\left(-\frac{\Delta G^{\ddagger}}{RT}\right)$$

Where $\Delta G^{\ddagger}$ is the activation free energy associated with interfacial adsorption or incorporation. For a curved interface, classical interfacial thermodynamics predicts that the interfacial free energy acquires curvature-dependent corrections. In the weak-curvature limit ($r \gg$ molecular length), the free energy can be expanded as

$$\Delta G^{\ddagger}(r) = \Delta G_{\infty} + \frac{C}{r}$$

consistent with Tolman-type curvature corrections and Helfrich curvature elasticity (Tolman, 1949; Capovilla et al., 2002). Substituting this expression into the activated uptake formulation yields

$$\alpha(r) \propto \exp\left(-\frac{\Delta G^{\ddagger}(\infty)}{k_B T}\right)\exp\left(-\frac{C}{k_B T r}\right)$$
$$\propto \alpha(\infty)\exp\left(-\frac{r_c}{r}\right)$$

Where r_c is a characteristic curvature length scale determined by interfacial tension and molecular restructuring at the interface.

In addition to curvature-modified interfacial reactivity, the overall uptake rate is further constrained by geometric and transport limitations. Following a two-film–type resistance framework, the finite surface-area availability (scaling with particle radius r) and a finite effective reaction–diffusion depth δ can be treated as independent limitations acting in series (Li et al., 2022). Here, δ represents an effective length scale that integrates near-surface diffusion, interfacial accommodation kinetics, and molecular restructuring within the condensed phase. These constraints can be combined into an effective length scale $r+\delta$, analogous to a Padé-type interpolation between surface-area-limited and transport-limited regimes.

Accordingly, the apparent heterogeneous rate constant can be approximated as

$$k \propto \frac{1}{r+\delta}\exp\left(-\frac{r_c}{r}\right)$$

This formulation recovers the correct limiting behaviors: for $r \gg \delta$, $k_{app} \sim 1/r$, consistent with surface-area control, whereas for $r \gg \delta$, the rate becomes insensitive to further size reduction due to transport and interfacial limitations. Differentiation of the above expression yields an optimal particle radius,

$$r_{opt} = \frac{r_c}{2}\left(1+\sqrt{1+4\delta/r_c}\right)$$

at which the enhancement from increasing surface area is balanced by curvature- and transport-induced suppression. An order-of-magnitude estimate for δ can be obtained by considering the diffusion of sulfate ions away from the interfacial reaction zone. The characteristic diffusion length is given by $\delta \sim (D\tau)^{1/2}$, D is the effective diffusion coefficient of sulfate in concentrated NaCl solution and τ is the characteristic time over which surface-generated sulfate contributes to the measured concentration increase. Under the experimental conditions, δ is expected to be significantly reduced relative to dilute aqueous solutions due to high ionic strength and ion–ion interactions, yielding values on the order of 10^{-10}–10^{-11} $m^2\ s^{-1}$. For reaction times of several seconds to tens of seconds, this results in diffusion lengths of approximately 100–300 nm. Using physically reasonable values of r_c (20–40 nm), consistent with curvature effects reported for inorganic and organic aerosol interfaces (Barclay

and Lukes, 2019), and δ (100–300 nm), representing effective mass-transfer and interfacial restructuring lengths, the predicted maximum in k_{app} occurs in the range of approximately 150–250 nm. This prediction is in excellent agreement with the experimentally observed transition in the apparent reaction rate constant.

Table 1 compares the kinetic data obtained in this study with those reported by Jing et al. (2023) and Zhang and Chan (2023). For micrometer-sized NaCl droplets, such as those investigated by Jing et al. (2023) and Zhang and Chan (2023), heterogeneous SO_2 oxidation proceeds predominantly under bulk-phase or diffusion-limited conditions. In this size regime, reactant concentrations remain sufficiently high during the early stages of the reaction, resulting in nearly constant reaction rates over time. In contrast, nanoscale droplets exhibit rapid reactant consumption and reach quasi-equilibrium on much shorter timescales, leading to a pronounced temporal evolution of reaction kinetics.

Although direct quantitative comparison between nano- and microscale systems is complicated by differences in surface area, diffusion length, and SO_2 exposure conditions, the substantially higher sulfate concentrations formed in submicrometer droplets within 1 h highlight the enhanced reactivity of nanoscale aerosols. Under the kinetic framework proposed here, the sulfate concentration produced in 400 nm droplets after 1 h corresponds to that achieved in micrometer-sized droplets only after substantially longer reaction times, underscoring the critical role of particle size in governing heterogeneous oxidation rates.

3.3 Influence of Aerosol Mixing State on Reaction Rates

The effect of increasing particle size on the reaction rate discussed above reflects the combined influence of surface-to-volume ratio and surface curvature. To qualitatively assess the role of surface-area-related limitations independent of curvature effects, a series of controlled experiments employing organic surface coatings was conducted. This approach aims does not strictly decouple geometric and interfacial effects, but provides a proxy for evaluating how reductions in effective reactive surface area influence reaction kinetics under otherwise comparable conditions. SOS was selected as the additive, representing organic sulfonates that constitute an important fraction of SOA, accounting for approximately 5 %–30 % of the total organic aerosol mass (Zhang et al., 2022). These compounds contain hydrophilic sulfate groups and exhibit surface activity. When mixed with inorganic salts, they can induce LLPS, which modifies the hygroscopicity, scattering properties, and material exchange between aerosols and the atmosphere (Zhang et al., 2022; Freedman, 2020). GF measurements were performed for binary NaCl-SOS particlesfollowing UV-induced SO_2 oxidation over different reaction times. Sulfate formation were subsequently derived in Fig. 6a and b.

The corresponding microscopic images of the binary particles with different organic volume fractions are presented in Figs. S13–S18, and the GF values derived from these binary single-particle images are summarized in Table S2. Binary particles consistently exhibited lower sulfate formation at a given reaction time compared to monodisperse NaCl particles with the same NaCl mass (Fig. 6a). The magnitude of this difference increases with increasing OVF, suggesting that the presence of the organic phase inhibits the heterogeneous reaction between NaCl and SO_2.

This inhibition is consistent with the formation of an organic coating on the surface of NaCl particle surface via LLPS, which introduces an additional barrier between the aqueous and gas phases. Importantly, the introduction of the organic phase alters not only the exposed reactive surface area but also the interfacial transport properties. Consequently, the observed kinetic suppression should be interpreted as the combined effect of reduced effective surface area and hindered interfacial transport. Nevertheless, the OVF-dependent trends provide insight into the relative importance of surface-area-related limitations. The samples tested, with an effective surface-to-volume ratio comparable to or greater than 100 nm monodisperse aerosols, exhibit a slower sulfate formation rate, confirming that an increase in surface-to-volume ratio is unfavorable for mass transfer. As the OVF increases from 0 %, the coverage of the NaCl droplet surface by the SOS layer expands reduces the fraction of exposed inorganic surface while leaving the particle curvature essentially unchanged. In this sense,the experiments approximate a scenario in which the effective reactive surface-area-to-volume ratio decreases without invoking curvature-related effects. In the low-OVF regime (OVF < 33 %), whereas a more pronounced decrease in k is observed at higher OVFs (Fig. 6b). This behavior is consistent with a transition from partial to more extensive surface coverage, although the exact coverage state cannot be uniquely determined from the present data. When compared with the particle-size-dependent trends observed for monodisperse NaCl aerosols, these results suggest that a reduction in effective surface-area-to-volume ratio alone leads to a decrease in the heterogeneous reaction rate. This contrasts with the increasing reaction rate observed for small monodisperse particles in the 50–200 nm size range, where reduced surface curvature is expected to facilitate gas uptake and interfacial transport. Taken together, these findings support the interpretation that curvature-related effects dominate the enhancement of reaction rates in the small-particle regime, whereas surface-area-related limitations become increasingly important once curvature effects are minimized.

4 Conclusion

In this work, we measured the UV catalyzed SO_2 conversion in nanometer-sized sea-salt aerosol droplets and con-

Table 1. Sulfate formation rates from heterogeneous oxidation of SO_2 in droplets of different sizes.

Reference	Medium	Catalyst	Conditions	Size	Sulfate formation of 1 h (10^{-3} mol L^{-1})
Zhang and Chan (2023)	NaCl	UV	6.5 ppm SO_2; PH = 7; 80 % RH	57 ± 2 µm	4.68
Jing et al. (2023)	NaCl	Mn(II)	1 ppm SO_2; PH = 5–8; 80 % RH	50 µm	36
				27 µm	43.5
				20 µm	54
				15 µm	72
				10 µm	108
				5 µm	216
The present study	NaCl	UV	200 ppm SO_2; PH = 7; 80 % RH	400 nm	1420
				300 nm	1841
				200 nm	2224
				100 nm	1404
				50 nm	894

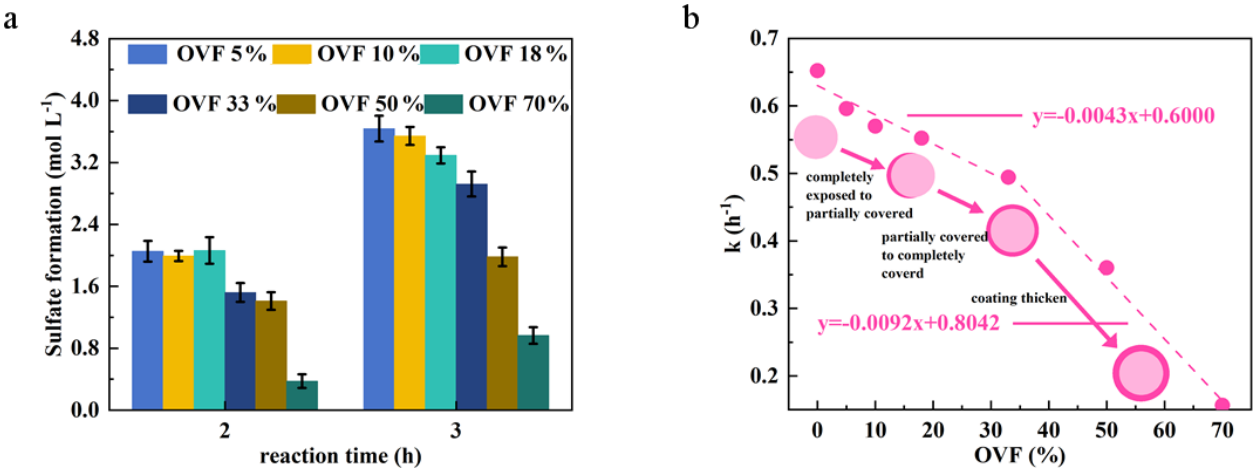

Figure 6. **(a)** Sulfate concentration of NaCl-SOS mixed particles with different OVFs after reaction times of 2 and 3 h, and **(b)** the corresponding reaction rate constants k.

firmed that hygroscopic measurements based on dark-field optical microscopy, combined with the ZSR model, can be utilized in inverting the heterogeneous reaction rate of single nanoparticles. We found that, at the nanoscale, the UV-catalyzed SO_2 oxidation in aerosol droplets follows a first-order reaction. In the small particle size range (< 200 nm), an increase in particle size positively influences the reaction rate, which is likely attributable to the inhibitory effect of increased surface curvature on the mass transfer rate. However, for particles larger than 200 nm, the decrease in surface-to-volume ratio limits mass transfer efficiency, and the reaction rate becomes negatively correlated with particle size. This suggests that the UV-catalyzed oxidation of sea-salt aerosols in the atmosphere exhibits a pronounced particle-size dependence, whereby particles within specific size ranges dominate sulfate production through this pathway relative to other size fractions. Additional measurements performed at 20 ppm SO_2 yielded qualitatively similar kinetic behavior, suggests that the elevated SO_2 concentration mainly affects the absolute reaction rate rather than the underlying kinetic behavior. Therefore, the particle-size and interfacial effects identified in this study are unlikely to be artifacts of the specific SO_2 concentration employed. The enhanced reactivity observed in nanoscale sea-salt aerosols suggests that heterogeneous sulfur oxidation in ultrafine marine particles may proceed more efficiently than predicted from bulk or micrometer-scale measurements. When nonreactive material forms a core-shell structure, the liquid outer layer can mask surface-active sites and effectively reduce the available specific surface area, thereby limiting mass transport and substantially suppressing the sulfate formation rate. Collectively, these findings provide new insights into the

mechanisms driving the rapid formation of nanoscale sulfate components during haze episodes and enhance our ability to predict how organic aerosols may indirectly influence atmospheric chemistry by altering the aerosol surface properties.

Code and data availability. The code and data are available upon request from the corresponding author (zbxie@aiofm.ac.cn).

Supplement. The supplement related to this article is available online at https://doi.org/10.5194/acp-26-12183-2026-supplement.

Author contributions. ZX designed the study. XX performed experiments. XW analyzed data. DZ helped with graphic visualization. HG and JL provided interpretation of results and financial support. XX wrote the manuscript with contributions from all coauthors.

Competing interests. The contact author has declared that none of the authors has any competing interests.

Disclaimer. Publisher's note: Copernicus Publications remains neutral with regard to jurisdictional claims made in the text, published maps, institutional affiliations, or any other geographical representation in this paper. The authors bear the ultimate responsibility for providing appropriate place names. Views expressed in the text are those of the authors and do not necessarily reflect the views of the publisher.

Acknowledgements. This work was Supported by the National Natural Science Foundation of China (42305143, 42375124), the Science and Technological Fund of Anhui Province (grant nos. 2308085QD128), the Research Team Construction Project of Hefei Comprehensive Science Center Environmental Research Institute (HYKYTD2024006).

Financial support. This research has been supported by the National Natural Science Foundation of China, Youth Science Fund Project (grant no. 42305143), the National Natural Science Foundation of China, Major Research Plan (grant no. 42375214), the Anhui Provincial Department of Science and Technology, Natural Science Foundation of Anhui Province (grant no. 2308085QD128), and the Research Team Construction Project of Hefei Comprehensive Science Center Environmental Research Institute (grant no. HYKYTD2024006).

Review statement. This paper was edited by Harald Saathoff and reviewed by two anonymous referees.

References

Angle, K. J., Neal, E. E., and Grassian, V. H.: Enhanced Rates of Transition-Metal-Ion-Catalyzed Oxidation of S(IV) in Aqueous Aerosols: Insights into Sulfate Aerosol Formation in the Atmosphere, Environ. Sci. Technol., 55, 10291–10299, https://doi.org/10.1021/acs.est.1c01932, 2021.

Barclay, P. L. and Lukes, J. R.: Curvature dependence of the mass accommodation coefficient, Langmuir, 35, 6196–6262, https://doi.org/10.1021/acs.langmuir.9b00537, 2019.

Bi, J., Huang, J., Hu, Z., Holben, B. N., and Guo, Z.: Investigating the aerosol optical and radiative characteristics of heavy haze episodes in beijing during january of 2013, J. Geophys. Res.-Atmos., 119, 9884–9900, https://doi.org/10.1002/2014JD021757, 2013.

Cao, X., Chen, Z., Liu, Y., Jing, X., Li, L., Liu, P., and Zhang, Y.: Directly Measuring Fe(III)-catalyzed SO_2 Oxidation Rate in Single Optically Levitated Droplets, Environ. Sci. Atmos., 3, 298–304, https://doi.org/10.1039/d2ea00125j, 2023.

Cao, X., Liu, Y., Huang, Q., Chen, Z., Sun, J., Sun, J., Pang, S., Liu, P., Wang, W., Zhang, Y., and Ge, M.: Single Droplet Tweezer Revealing the Reaction Mechanism of Mn(II)-Catalyzed SO_2 Oxidation, Environ. Sci. Technol., 58, 5068–5078, https://doi.org/10.1021/acs.est.4c00309, 2024a.

Cao, Y., Li, Y., Wang, X., Ma, Q., Zhang, C., Zhang, P., Chen, T., Wang, Y., Chu, B., Zhang, X., Francisco, J. S., and He, H.: Photoactivation of chloride by oxygen in aqueous aerosols drives sulfate formation, J. Am. Chem. Soc., 146, 1467–1475, https://doi.org/10.1021/jacs.3c10840, 2024b.

Capovilla, R., Guven, J., and Santiago, J. A.: Lipid membranes with an edge, Phys. Rev. E, 66, 021607, https://doi.org/10.1103/PhysRevE.66.021607, 2002.

Carslaw, K. S., Boucher, O., Spracklen, D. V., Mann, G. W., Rae, J. G. L., Woodward, S., and Kulmala, M.: A review of natural aerosol interactions and feedbacks within the Earth system, Atmos. Chem. Phys., 10, 1701–1737, https://doi.org/10.5194/acp-10-1701-2010, 2010.

Chan, M. N. and Chan, C. K.: Mass transfer effects in hygroscopic measurements of aerosol particles, Atmos. Chem. Phys., 5, 2703–2712, https://doi.org/10.5194/acp-5-2703-2005, 2005.

Chi, J. W., Li, W. J., Zhang, D. Z., Zhang, J. C., Lin, Y. T., Shen, X. J., Sun, J. Y., Chen, J. M., Zhang, X. Y., Zhang, Y. M., and Wang, W. X.: Sea salt aerosols as a reactive surface for inorganic and organic acidic gases in the Arctic troposphere, Atmos. Chem. Phys., 15, 11341–11353, https://doi.org/10.5194/acp-15-11341-2015, 2015.

Cui, X., Wang, X., Yang, L., Chen, B., Chen, J., Andersson, A., and Gustafsson, Ö.: Radiative absorption enhancement from coatings on black carbon aerosols, Sci. Total Environ., 551, 51–56, https://doi.org/10.1016/j.scitotenv.2016.02.026, 2016.

Davies, J. F., Zuend, A., and Wilson, K. R.: Technical note: The role of evolving surface tension in the formation of cloud droplets, Atmos. Chem. Phys., 19, 2933–2946, https://doi.org/10.5194/acp-19-2933-2019, 2019.

Finlayson-Pitts, B. J. and Hemminger, J. C.: Physical chemistry of airborne sea salt particles and their components, J. Phys. Chem. A., 104, 11463–11477, https://doi.org/10.1021/jp002968n, 2000.

Freedman, M. K.: Phase Separation in Organic Aerosol, Chem. Soc. Rev., 46, 7694, https://doi.org/10.1039/c6cs00783j, 2017.

Freedman, M. K.: Liquid–Liquid Phase Separation in Supermicrometer and Submicrometer Aerosol Particles, Acc. Chem. Res., 53, 1102–1110, https://doi.org/10.1021/acs.accounts.0c00093, 2020.

Gen, M., Zhang, R., Li, Y., and Chan, C.: Multiphase Photochemistry of Iron-Chloride Containing Particles as a Source of Aqueous Chlorine Radicals and Its Effect on Sulfate Production, Environ. Sci. Technol., 54, 9862–9871, https://doi.org/10.1021/acs.est.0c01540, 2020.

Gong, X., Zhang, J., Croft, B., Yang, X., Frey, M., Bergner, N., Chang, R. Y., Creamean, J. M., Kuang, C. A., Martin, R. V., Ranjithkumar, A., Sedlacek, A. J., Uin, J., Willmes, S., Zawadowicz, M. A., Pierce, J. R., Shupe, M. D., Schmale, J., and Wang, J.: Arctic warming by abundant fine sea salt aerosols from blowing snow, Nat. Geosci., 16, 768–774, https://doi.org/10.1038/s41561-023-01254-8, 2023.

Jing, X., Chen, Z., Cao, X., Huang, Q., Liu, P., and Zhang, Y.: Rapid Sulfate Formation via Mn^{2+}-Catalyzed SO_2 Oxidation on the Surface of NaCl Microdroplets, J. Phys. Chem. C., 127, 13632–13638, https://doi.org/10.1021/acs.jpcc.3c02839, 2023.

Kaku, K. C., Hegg, D. A., Covert, D. S., Santarpia, J. L., Jonsson, H., Buzorius, G., and Collins, D. R.: Organics in the Northeastern Pacific and their impacts on aerosol hygroscopicity in the subsaturated and supersaturated regimes, Atmos. Chem. Phys., 6, 4101–4115, https://doi.org/10.5194/acp-6-4101-2006, 2006.

Keene, W. C., Sander, R., Pszenny, A. A. P., Vogt, R., Crutzen, P. J., and Galloway, J. N.: Aerosol pH in the marine boundary layer: A review and model evaluation, J. Aerosol Sci., 29, 339–356, https://doi.org/10.1016/s0021-8502(97)10011-8, 1998.

Kuai, Y., Chen, J., Tang, X., Xiang, Y., Lu, F., Kuang, C., Xu, L., Shen, W., Cheng, J., Gui, H., Zou, G., Wang, P., Ming, H., Liu, J., Liu, X., Lakowicz, J. R., and Zhang, D. G.: Label-free surface-sensitive photonic microscopy with high spatial resolution using azimuthal rotation illumination, Sci. Adv., 5, eaav5335, https://doi.org/10.1126/sciadv.aav5335, 2019.

Kuai, Y., Xie, Z., Chen, J., Gui, H., Xu, L., Kuang, C., Wang, P., Liu, X., Liu, J., Lakowicz, J. R., and Zhang, D. G.: Real-Time Measurement of the Hygroscopic Growth Dynamics of Single Aerosol Nanoparticles with Bloch Surface Wave Microscopy, ACS Nano., 14, 9136–9144, https://doi.org/10.1021/acsnano.0c04513, 2020.

Laskin, A., Moffet, R., Gilles, M., Fast, J., Zaveri, R., Wang, B., Nigge, P., and Shutthanandan, J.: Tropospheric chemistry of internally mixed sea salt and organic particles: Surprising reactivity of NaCl with weak organic acids, J. Geophys. Res.-Atmos., 117, D15302, https://doi.org/10.1029/2012JD017743, 2012.

Li, G., Su, H., Li, M., Kuhn, U., Zheng, G., Han, L., Bao, F., Pöschl, U., and Cheng, Y.: Reactive uptake coefficients for multiphase reactions determined by a dynamic chamber system, Atmos. Meas. Tech., 15, 6433–6446, https://doi.org/10.5194/amt-15-6433-2022, 2022.

Li, L., Liu, P., Huang, Q., Zhang, X., Chao, X., Pang, S., Wang, W., Cheng, Y., Su, H., Zhang, Y., and Ge, M.: Rethinking urban haze formation: Atmospheric sulfite conversion rate scales with aerosol surface area, not volume, One Earth, 7, 1082–1095, https://doi.org/10.1016/j.oneear.2024.05.007, 2024.

Liu, T. and Abbatt, J. P. D.: Oxidation of sulfur dioide by nitrogen dioxide accelerated at the interface of deliquesced aerosol particles, Nat. Chem., 13, 1173–1177, https://doi.org/10.1038/s41557-021-00777-0, 2021.

Liu, T., Clegg, S. L., and Abbatt, J. P. D.: Fast oxidation of sulfur dioxide by hydrogen peroxide in deliquesced aerosol particles, P. Natl. Acad. Sci. USA, 117, 1354–1359, https://doi.org/10.1073/pnas.1916401117, 2020.

Ma, J., Chen, Y., Wang, W., Yan, P., Liu, H., Yang, S., Hu, Z., and Lelieveld, J.: Strong air pollution causes widespread haze-clouds over China, J. Geophys. Res.-Atmos., 115, D18204, https://doi.org/10.1029/2009JD013065, 2010.

Murphy, D. M., Froyd, K. D., Bian, H., Brock, C. A., Dibb, J. E., DiGangi, J. P., Diskin, G., Dollner, M., Kupc, A., Scheuer, E. M., Schill, G. P., Weinzierl, B., Williamson, C. J., and Yu, P.: The distribution of sea-salt aerosol in the global troposphere, Atmos. Chem. Phys., 19, 4093–4104, https://doi.org/10.5194/acp-19-4093-2019, 2019.

Persad, G. G.: The dependence of aerosols' global and local precipitation impacts on the emitting region, Atmos. Chem. Phys., 23, 3435–3452, https://doi.org/10.5194/acp-23-3435-2023, 2023.

Rosati, B., Christiansen, S., Dinesen, A., Roldin, P., Massling, A., Nilsson, E.D., and Bilde, M.: The impact of atmospheric oxidation on hygroscopicity and cloud droplet activation of inorganic sea spray aerosol, Sci. Rep., 11, 10008, https://doi.org/10.1038/s41598-021-89346-6, 2021.

Rossi, M. J.: Heterogeneous reactions on salts, Chem. Rev., 103, 4823–4882, https://doi.org/10.1021/cr020507n, 2003.

Shang, D., Peng, J., Guo, S., Wu, Z., and Hu, M.: Secondary aerosol formation in winter haze over the Beijing-TianjinHebei Region, China, Front. Environ. Sci. Eng., 15, 1–13, https://doi.org/10.1007/s11783-020-1326-x, 2021.

Shiraiwa, M., Pfrang, C., and Pöschl, U.: Kinetic multi-layer model of aerosol surface and bulk chemistry (KM-SUB): the influence of interfacial transport and bulk diffusion on the oxidation of oleic acid by ozone, Atmos. Chem. Phys., 10, 3673–3691, https://doi.org/10.5194/acp-10-3673-2010, 2010.

Soni, M., Sander, R., Sahu, L. K., Taraborrelli, D., Liu, P., Patel, A., Girach, I. A., Pozzer, A., Gunthe, S. S., and Ojha, N.: Comprehensive multiphase chlorine chemistry in the box model CAABA/MECCA: implications for atmospheric oxidative capacity, Atmos. Chem. Phys., 23, 15165–15180, https://doi.org/10.5194/acp-23-15165-2023, 2023.

Su, B., Wang, T., Zhang, G., Liang, Y., Lv, C., Hu, Y., Li, L., Zhou, Z., Wang, X. M., and Bi, X. H.: A review of atmo-spheric aging of sea spray aerosols:Potential factor saffecting chlorid edepletion, Atmos. Environ., 290, 119365, https://doi.org/10.1016/j.atmosenv.2022.119365, 2022.

Tolman, R. C.: The effect of droplet size on surface tension, J. Chem. Phys., 17, 333–337, https://doi.org/10.1063/1.1747247, 1949.

Wang, W., Liu, M., Wang, T., Song, Y., Zhou, L., Cao, J., Hu, J., Tang, G., Chen, Z., Li, Z., Xu, Z., Peng, C., Lian, C., Chen, Y., Pan, Y., Zhang, Y., Sun, Y., Li, W., Zhu, T., Tian, H., and Ge, M.: Sulfate Formation is Dominated by ManganeseCatalyzed Oxidation of SO_2 on Aerosol Surfaces During Haze Events, Nat. Commun., 12, 1993, https://doi.org/10.1038/s41467-021-22091-6, 2021.

Wang, X., Jacob, D. J., Eastham, S. D., Sulprizio, M. P., Zhu, L., Chen, Q., Alexander, B., Sherwen, T., Evans, M. J., Lee, B. H., Haskins, J. D., Lopez-Hilfiker, F. D., Thornton, J. A.,

Huey, G. L., and Liao, H.: The role of chlorine in global tropospheric chemistry, Atmos. Chem. Phys., 19, 3981–4003, https://doi.org/10.5194/acp-19-3981-2019, 2019.

Wang, Z., Jing, B., Shi, X., Tong, S., Wang, W., and Ge, M.: Importance of water-soluble organic acid on the hygroscopicity of nitrate, Atmos. Environ., 190, 65–73, https://doi.org/10.1016/j.atmosenv.2018.07.010, 2018.

Xie, Z., Kuai, Y., Liu, J., Gui, H., Zhang, J., Dai, H., Xiao, H., Chen, D., and Zhang, D.: In situ quantitative observation of hygroscopic growth of single nanoparticle aerosol by surface plasmon resonance microscopy, Anal. Chem., 92, 11062–11071, https://doi.org/10.1021/acs.analchem.0c00431, 2020.

Xie, Z., Gui H., Zhang, J., Yang, B., Kang, S., Wei, X., Yu, T., Yang, Y., Liu, J., and Liu, W.: Measurement techniques new progress of atmospheric fine particles, Energy Environ. Prot., 37, 16–29, https://doi.org/10.20078/j.eep.20230308, 2023.

Yang, B., Xie, Z., Liu, J., Gui, H., Zhang, J., Wei, X., Wang, J., Fan, Z., and Zhang, D.: Investigating the hygroscopicities of calcium and magnesium salt particles aged with SO_2 using surface plasmon resonance microscopy, Sci. Total Environ., 867, 161588, https://doi.org/10.1016/j.scitotenv.2023.161588, 2023.

Zangmeister, C. and Pemberton, J.: Raman Spectroscopy and Atomic Force Microscopy of the Reaction of Sulfuric Acid with Sodium Chloride, J. Am. Chem. Soc., 122, 12289–12296, https://doi.org/10.1021/ja001469x, 2000.

Zhang, H., Xu, Y., and Jia, L.: A chamber study of catalytic oxidation of SO_2 by Mn^{2+}/Fe^{3+} in aerosol water, Atmos. Environ., 245, 118019, https://doi.org/10.1016/j.atmosenv.2020.118019, 2021.

Zhang, J., Wang, Y., Teng, X., Liu, L., Xu, Y., Ren, L., Shi, Z.,Zhang, Y., Jiang, J., Liu, D., Hu, M., Shao, L., Chen, J., Martin, S., Zhang, X., and Li, W.: Liquid-liquid Phase Separation Reduces Radiative Absorption by Aged Black Carbon Aerosols, Comun. Earth Environ., 3, 128, https://doi.org/10.1038/s43247-022-00462-1, 2022.

Zhang, R. and Chan, C. K.: Simultaneous formation of sulfate and nitrate via co-uptake of SO_2 and NO_2 by aqueous NaCl droplets: combined effect of nitrate photolysis and chlorine chemistry, Atmos. Chem. Phys., 23, 6113–6126, https://doi.org/10.5194/acp-23-6113-2023, 2023.